Supplemental Information

Solvation Geometry Engineering for Stable High-Voltage Potassium-Ion Batteries

Zhe Zhang[ad]†, Wenli Qi[b]†, Shiwan Zhang[a]†, Jiacheng Zhu[e], Linlin Wang[a], Yue Bai[a], Jiale Chen[a], Yifan Chen[a], Guangqiang Hou[a], Xiaogang Niu[a], Xuefeng Wang[e*], Jitao Chen[d*], Xiao Ji[c*] and Yujie Zhu[a*]

[a]*School of Chemistry, Beihang University, Beijing 100191, China.* [*]*E-mail: yujiezhu@buaa.edu.cn*

[b]*China-EU Institute for Clean and Renewable Energy, Huazhong University of Science and Technology, Wuhan, Hu-bei 430074, P. R. China.*

[c]*School of Optical and Electronic Information, Huazhong University of Science and Technology, Wuhan, Hubei 430074, P. R. China.* [*]*E-mail: jixiao@hust.edu.cn*

[d]*Beijing National Laboratory for Molecular Sciences, College of Chemistry and Molecular Engineering, Peking University, Beijing 100871, P. R. China.* [*]*E-mail: chenjitao@pku.edu.cn*

[e]*Institute of Physics, Chinese Academy of Sciences; College of Materials Science and Opto-Electronic Technology, University of Chinese Academy of Sciences, Beijing 100190, P. R. China.* [*]*E-mail: wxf@iphy.ac.cn*

† These authors contributed equally to this work.

Materials and Electrolytes

Diethylene glycol dimethyl ether (DEGDME, 99.5%), diethylene glycol dibutyl ether (DEGDBE, 99%), and triethylene glycol dimethyl ether (TEGDME, 99%) were purchased from Beijing InnoChem Science & Technology Co., Ltd. Diethylene glycol ethyl methyl ether (DEGMEE, 98%), diethylene glycol diethyl ether (DEGDEE, 98%), and dipropylene glycol dimethyl ether (DPGDME, 99.1%) were purchased from Shanghai aladdin Biochemical Technology Co.,Ltd. Dipropylene glycol methyl propyl ether (DPGMPE, 99%) was purchased from Zhengzhou Alfa Chemical Co., Ltd. Ethylene carbonate (EC)/diethyl carbonate (DEC) (1:1 by volume) and potassium bis(fluoromenthanesulfonyl)imide (KFSI, 99.5%) were purchased from Suzhou Duoduo Chemical Technology Co., Ltd. N-methyl-2-pyrrolidone (NMP, 98%) was purchased from Shanghai Macklin Biochemical Co., Ltd. Graphite powder, hard carbon (HC) powder, carboxymethyl cellulose (CMC), and polyvinylidene fluoride (PVDF) were purchased from Shenzhen Kejing STAR Technology Company. Carbon nanotubes were purchased from Guangdong Canrd New Energy Technology Co., Ltd. All chemicals were used as received. $K_2Mn[Fe(CN)_6]$ (KMF) was synthesized following our reported method.[1] Electrolytes were prepared in an Ar-filled glovebox (<0.1 ppm H_2O/O_2) by dissolving stoichiometric amounts of KFSI in the corresponding solvents. For instance, 2.192 g of KFSI was added to 5 ml of the specific solvent under magnetic stirring to prepare a 2.0 M electrolyte.

Electrochemical Measurements

Graphite and HC electrodes were fabricated by coating an aqueous slurry (graphite/HC : CMC = 95 : 5 by weight) onto aluminum foil. KMF electrodes were prepared by coating an NMP slurry (KMF : PVDF : carbon nanotube = 80 : 10 : 10 by weight) onto aluminum foil. The wet coating thickness was controlled at 100-200 μm for graphite/HC slurries and 300-400 μm for KMF slurry. All coated electrodes were vacuum-dried at 80 °C for 4 h. The electrodes were then die-cut into 11 mm diameter discs and stored in an Ar-filled glove box. For half-cell assembly, the nominal areal loading was 1.5-2.0 mg cm^{-2} for graphite/HC electrodes and 3.0-4.0 mg cm^{-2} for KMF electrodes. For full-cells, the KMF electrode-to-graphite electrode mass ratio was maintained at ~2.1, while the KMF electrode-to-HC electrode mass ratio was ~2.5. Potassium metal electrodes were prepared by rolling a K slug into 0.5-mm-thick sheets, followed by punching 13-mm-diameter discs. Purification and anti-oxidation measures for potassium metal were taken from the reported literature.[2]

All coin cells (CR-2032 type) were assembled in an Ar-filled glovebox (<0.1 ppm H_2O/O_2) with a 0.5 mm thick spacer and a 1.8 mm thick spring. Half-cells employed a glass microfiber filter paper (Whatman, Grade GF/D, 16 mm diameter) as the separator, while full-cells utilized a microporous polypropylene film (Celgard 2500, 19 mm diameter) as the separator. Glass microfiber filters were used in half-cells to suppress potassium anode

dendrite growth, as their high thickness and porosity prevent dendrite penetration and enhance cycling stability. Microporous polypropylene films served in full-cells, owing to excellent mechanical strength, chemical compatibility and dense pore structure that ensures ion transport matching full-cell kinetics. Each coin cell was injected with 50 μL of electrolyte to ensure complete infiltration of the cell components and then left at open circuit for 4 hours before testing. The pouch cell was constructed in a double-layer configuration with an electrode area of 6 × 6 cm^2, active material loadings of ~15.5 and ~7.4 mg cm^{-2} for the cathode and anode, respectively, and an electrolyte dosage of 500 μL. Galvanostatic charge-discharge tests were performed using the Land battery testing system (CT2001A, Wuhan, China) and the Neware battery test system (CT-4008T, Shenzhen, China) with temperature controlled by an incubator (SPX-150BIII). At the room temperature (25 ± 0.5 °C), the test voltage ranges were: 0.01-2.0 V for the graphite||K and HC||K cells, 2.7-4.3 V for the KMF||K cells, and 1.5-4.2 V for the KMF||graphite and KMF||HC cells, respectively. At elevated temperatures (40 °C and 50 °C), the test voltage range of the KMF || graphite and KMF || HC cells was 1.5-4.1 V. The 1 C current rate is defined as 279 and 155 mA g^{-1} for the graphite||K and KMF||K, respectively, with calculations based on the weight of graphite and KMF in the corresponding cells. For the graphite||KMF and HC||KMF full-cells, both the specific current and specific capacity were calculated based on the mass of KMF in the cells. Before the long-term cycling stability tests at room and high temperatures, both the graphite||KMF and HC||KMF full-cells were cycled at 0.1 C for 20 times. Linear sweep voltammetry (LSV) and electrochemical impedance spectroscopy (EIS) measurements were performed using a Solartron Analytical electrochemical workstation (1470E, Solartron Mobrey, UK). LSV tests were executed on the K||Al cells with Al foil as the working electrode at a scan rate of 1 mV s^{-1} up to a termination potential of 7.0 V (*vs.* K^+/K). EIS was performed over a frequency range of 10^6 to 10^{-2} Hz with an oscillation amplitude of 10 mV. Leakage current tests were conducted using the KMF||K cells. The electrolyte-dependent K^+/K potential was characterized using a three-electrode coin cell with platinum working and counter electrodes, and a potassium metal reference electrode. 50 mM ferrocene was added to the electrolyte for potential calibration.

Materials Characterizations

The conductivity of electrolytes was measured using a DDS-307A conductivity meter at room temperature. To reduce statistical uncertainty, triplicate measurements were conducted for every sample, and the average values were used. The flash point, melting point, and boiling point of DPGMPE were determined at Hefei Guangce Product Testing Institute Co., Ltd. using test methods GB/T 21790-2008, GB/T 617-2006, and GB/T 7534-2004, respectively. Raman spectroscopy for the electrolytes was performed on a Horiba LabRAM HR Evolution system, employing a 633 nm excitation laser (5.1 mW power) over

the 400-2000 cm^{-1} range. Nuclear magnetic resonance (NMR) for the electrolytes was conducted by a Bruker Avance III HD 500 MHz spectrometer using C_2D_6SO as the deuterated reagent. To prevent interference from the deuterated solvent, the electrolyte was sealed in a 3 mm NMR tube. This tube was then inserted into a 5 mm NMR tube, and the annular space was filled with C_2D_6SO. Thermogravimetric analyses (TGA) were performed using a HITACHI STA200 thermogravimetric analyzer with a heating rate of 10 °C min^{-1} under an Ar atmosphere. Scanning electron microscopy (SEM) was performed with a JSM-7500F field emission scanning electron microscope at 10 kV. X-ray photoelectron spectroscopy (XPS) measurements were performed using a Thermo Scientific ESCA-LAB 250 Xi XPS system with a monochromatic Al Kα X-ray radiation (1361 eV) within a spot size of 400 μm in diameter, and the binding energy was calibrated by setting the C 1s peak position of adventitious carbon to 284.8 eV. Time-of-flight secondary ion mass spectrometry (ToF-SIMS) analysis was performed using a PHI NANO TOF 3 instrument. A 1 keV Cs^+ ion beam was used for sputtering, followed by a 30 keV Bi^{3+} primary ion beam for acquisition, with typical sputtered and analyzed areas of 400 μm × 400 μm and 200 μm × 200 μm, respectively. Cryogenic transmission electron microscopy (cryo-TEM) was performed on a JEOL JEM-F200 instrument operating at 200 kV. Electrode-active material was scraped from the cycled graphite anodes within an Ar-filled glovebox, gently pulverized, and deposited onto TEM grids via electrostatic adsorption. To prevent air exposure, grids were loaded into a cryogenic transfer holder (Fischione model 2550) with sealed shutters maintaining an argon atmosphere. The holder was subsequently inserted into the TEM column, and liquid nitrogen was introduced into its Dewar flask to achieve a stabilized temperature of 95.15 K prior to imaging. For sample post-analysis, including XRD, SEM, XPS, ToF-SIMS, and cryo-TEM measurements, samples were prepared by dissembling the corresponding coin-type half- or full-cells cycled at 0.1 C for 20 cycles in an Ar-filled glovebox to obtain the cycled electrodes, with the exception of SEM samples for characterizing aluminum surface morphology, which were obtained after five cycles of LSV tests. To remove residual electrolyte, the electrodes were rinsed using DEGDME and dried prior to further characterizations.

Computational Methods

Quantum Chemical Calculations

Density functional theory (DFT) calculations were performed using the Gaussian 16 program[3]. The geometries of solvent molecules were fully optimized at the B3LYP[4]/6-31+G(d) level. Single-point energy calculations were then carried out with the 6-311++G(d,p) basis set to obtain the wave functions. The binding energy (E_b) between a solvent molecule and K-ion was calculated to evaluate their interaction strength, defined as:

$$E_b = E_{xy} - E_x - E_y$$

In this equation, E_b denotes the total energy of the K^+-solvent complexes, E_x and E_y represent the single point energies of components x and y, respectively. The computed E_b primarily reflects the electrostatic (ion–dipole) interactions within the complex.

The molecular orbital energies, specifically the highest occupied molecular orbital (HOMO) and the lowest unoccupied molecular orbital (LUMO), of the solvents and salts were analyzed using the Multiwfn software[5] based on the obtained results. Electrostatic potential maps were generated using Multiwfn[5] and VMD software[6].

Electrolyte Structure Simulations

Molecular dynamic (MD) simulations were conducted on the electrolytes using the Large-scale Atomic/Molecular Massively Parallel Simulator (LAMMPS, http://lammps.sandia.gov.) package[7]. The all-atom optimized potentials for liquid simulations (OPLS-AA) force-field, incorporating description for the K^+ and FSI^- sourced from previous publications[8, 9]. The force-fields for DEGDME, DPGDME, and DPGMPE were obtained from the LigParGen[10]. The electrolyte systems were initially set up with the distribution of salt and solvent molecules in simulation boxes using Packmol[11] and Moltemplate (http://www.moltemplate.org/)[12]. The RESP2(0.5) charges for all organic solvent molecules and anions were calculated using the Multiwfn software[13]. For each system, an initial energy minimization at 0 K was performed (energy and force tolerances of 10^{-5}) to reach the ground-state structure. The system was then heated from 0 K to room temperature (300 K) at constant volume over 0.2 ns using a Langevin thermostat with a damping parameter of 100 ps. This was followed by equilibration in the NPT ensemble (constant temperature of 300 K and constant pressure of 1 bar) for 10 ns. Subsequently, an NVT ensemble MD simulation was conducted for 5 ns for further equilibration, followed by a final 15 ns NVT production run for data analysis. Visualization of the structures was made by using VESTA[14] and VMD software[6].

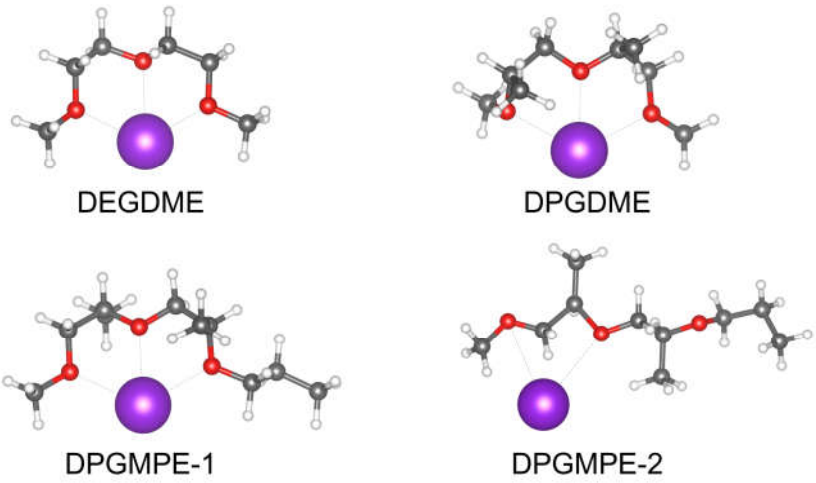

Figure S1. The optimized binding configurations of various solvent molecules with K^+.

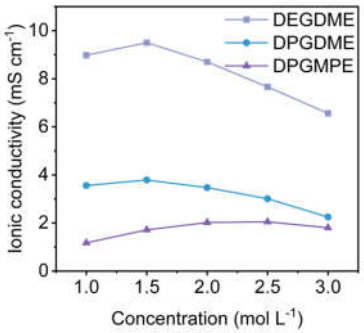

Figure S2. Concentration-dependent ionic conductivity of DEGDME, DPGDME, and DPGMPE electrolytes measured at room temperature over a concentration range of 1.0 to 3.0 M.

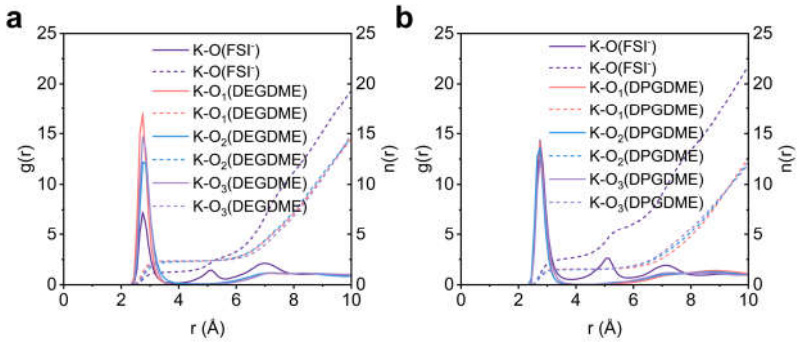

Figure S3. Radial distribution functions from MD simulations for the (a) DEGDME and (b) DPGDME electrolytes.

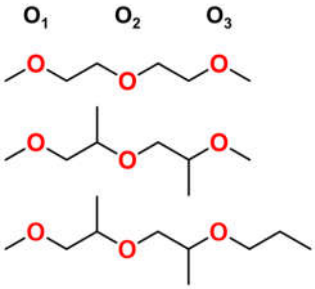

Figure S4. Representative molecular structures of DEGDME, DPGDME, and DPGMPE with the O_1, O_2, and O_3 atoms labeled.

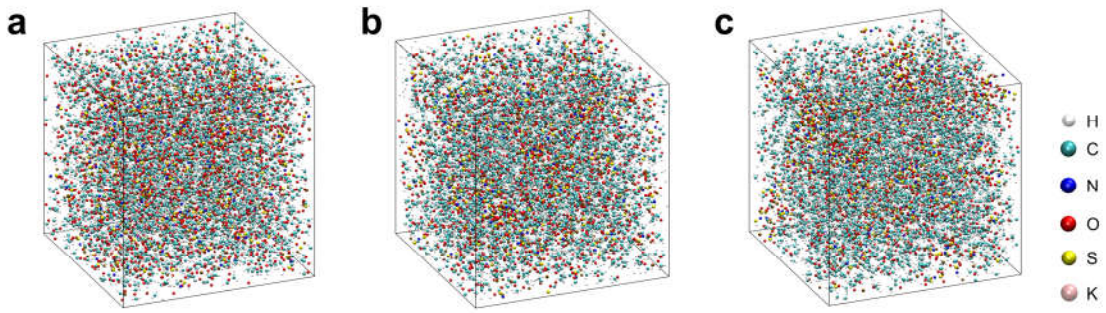

Figure S5. Representative MD simulation snapshots in (a) DEGDME, (b) DPGDME, and (c) DPGMPE electrolytes.

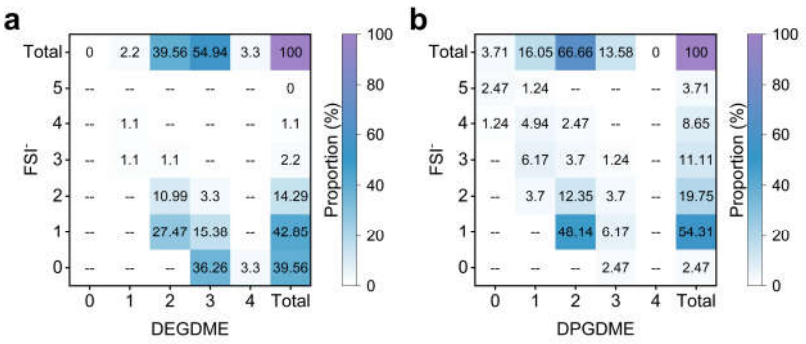

Figure S6. Proportion of K-ion solvation structures in the DEGDME and DPGDME electrolytes.

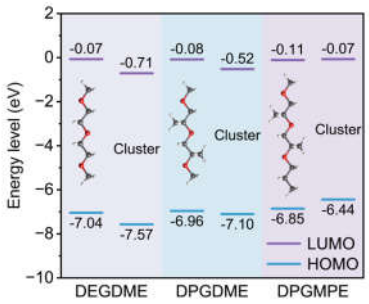

Figure S7. HOMO and LUMO levels of different molecules and clusters from DFT calculations.

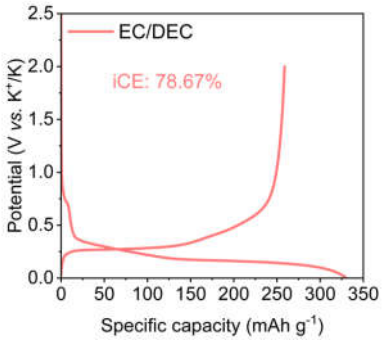

Figure S8. Initial galvanostatic charge-discharge profile of the graphite anode in the EC/DEC electrolyte at 0.1 C.

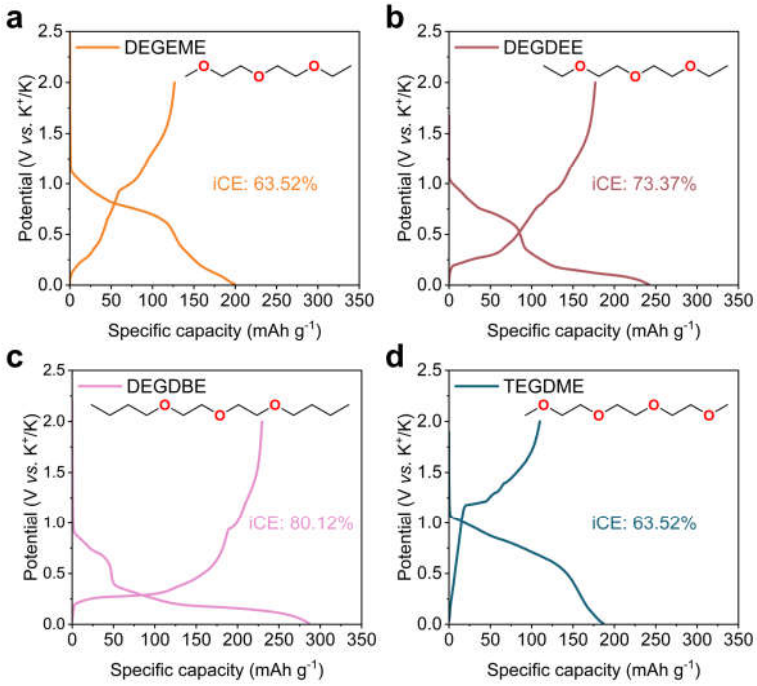

Figure S9. Initial galvanostatic charge-discharge profiles of the graphite anode in the (a) DEGMEE, (b) DEGDEE, (c) DEGDBE, and (d) TEGDME electrolyte at 0.1 C.

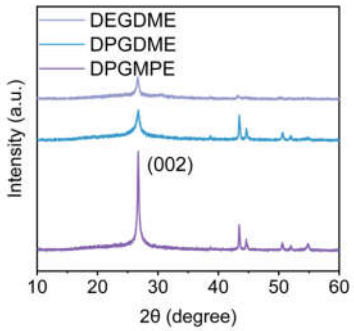

Figure S10. *Ex situ* XRD results of the graphite anode after cycling in the DEGDME, DPGDME, and DPGMPE electrolytes.

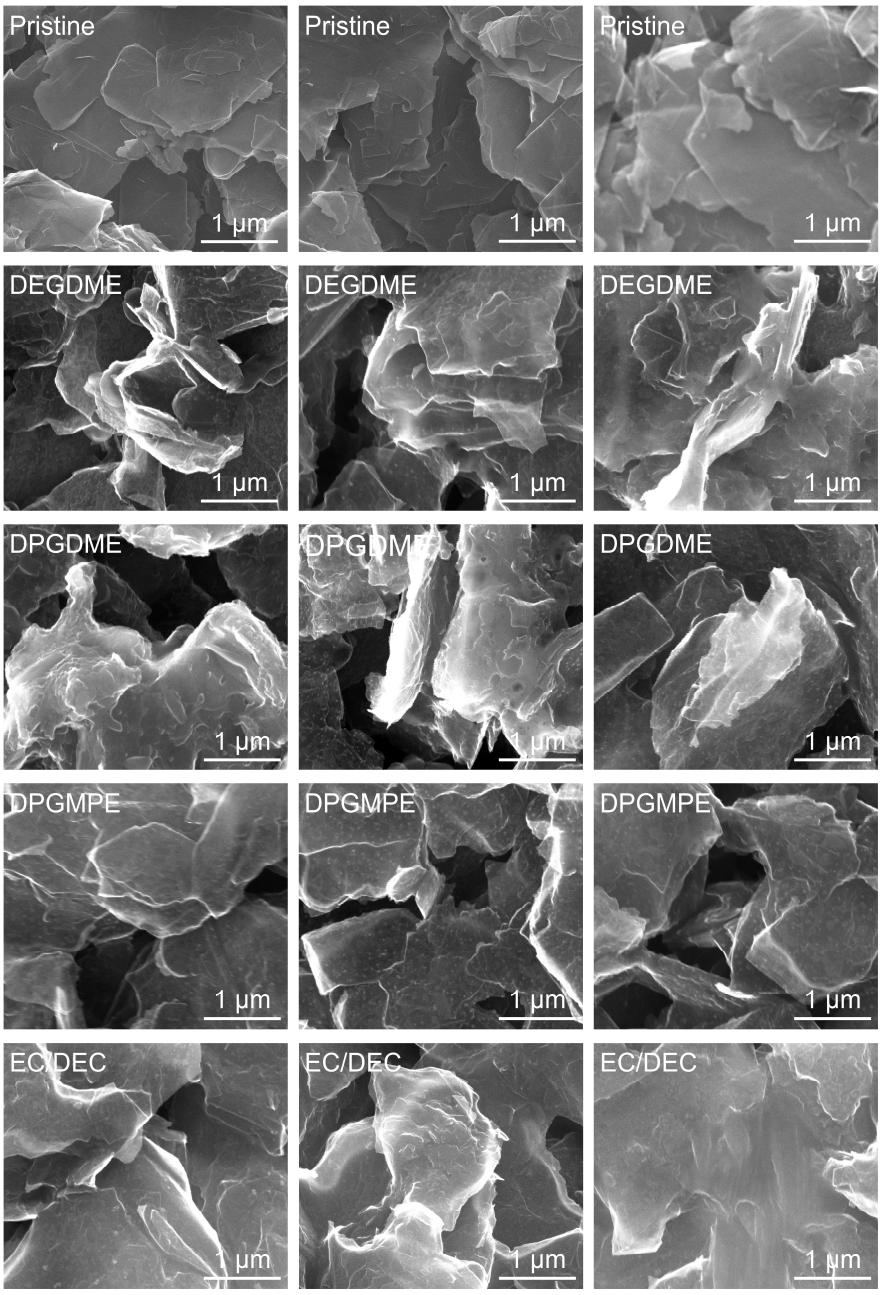

Figure S11. Comparison of SEM images of the graphite anode in the pristine state and after cycling in DEGDME, DPGDME, DPGMPE, and EC/DEC electrolytes.

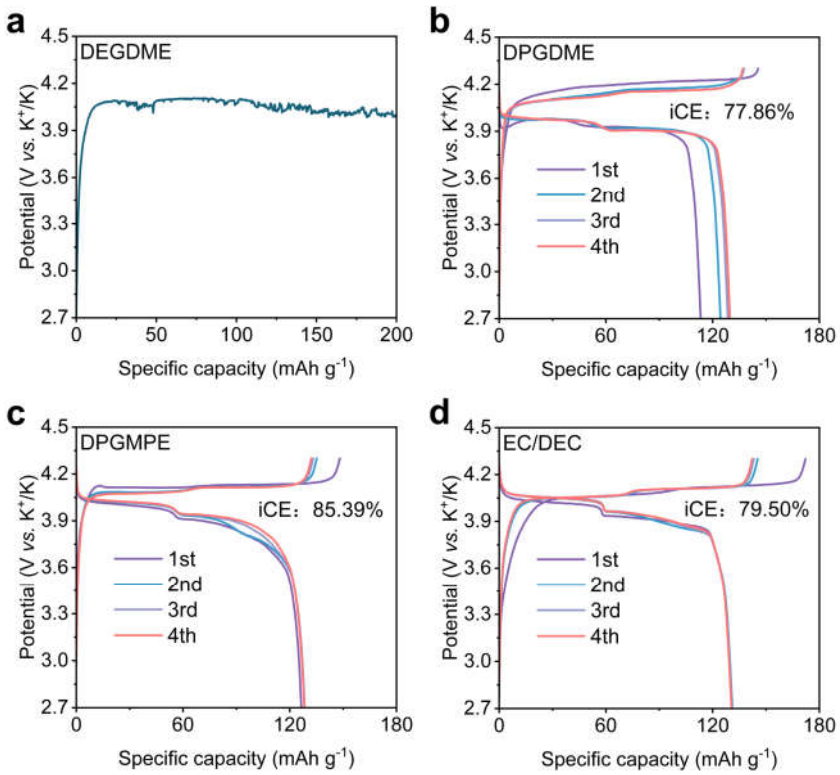

Figure S12. Comparison of galvanostatic charge-discharge profiles of the KMF cathode in the (a) DEGDME, (b) DPGDME, (c) DPGMPE, and (d) EC/DEC electrolyte at 0.1 C.

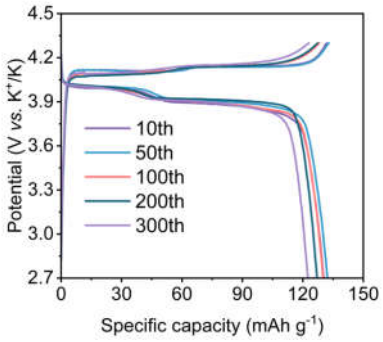

Figure S13. Galvanostatic charge-discharge curves of the KMF||K cell in the DPGMPE electrolyte at 0.1 C.

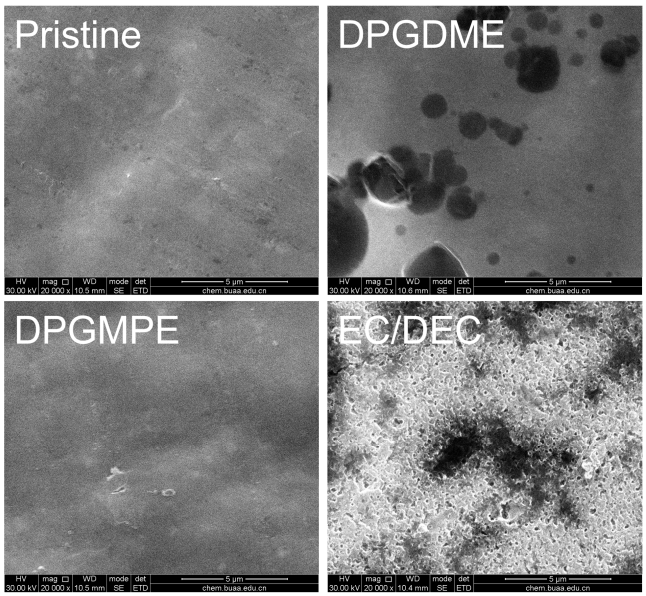

Figure S14. Comparison of SEM images of Al current collectors in the pristine state and those after LSV tests with different electrolytes.

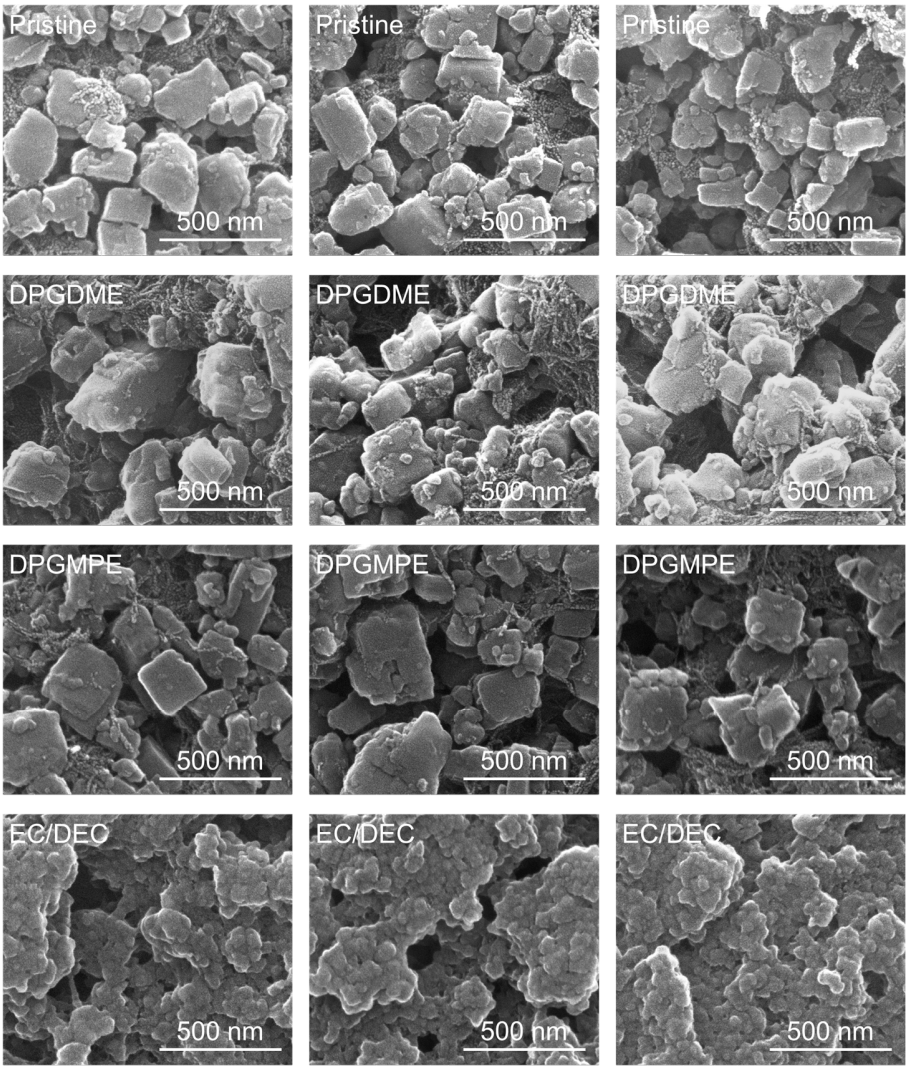

Figure S15. Comparison of SEM images of the KMF cathode in the pristine state and after cycling in DPGDME, DPGMPE, and EC/DEC electrolytes.

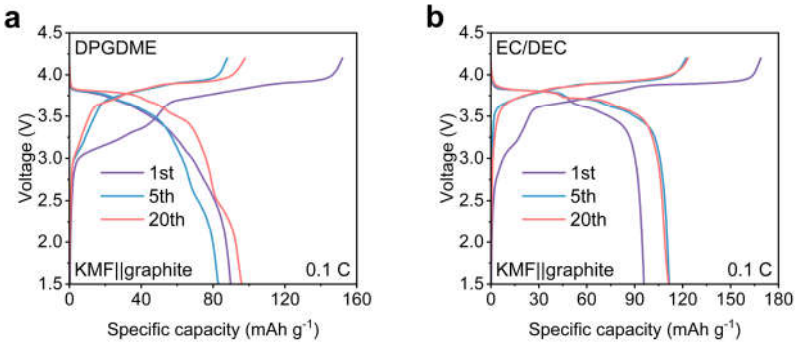

Figure S16. Galvanostatic charge-discharge curves of the KMF||graphite full-cells in (a) DPGDME and (b) EC/DEC electrolytes at 0.1 C.

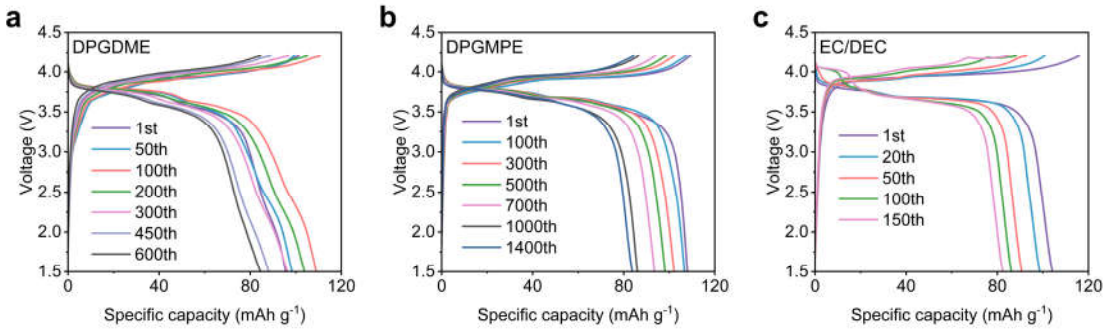

Figure S17. Comparison of galvanostatic charge-discharge curves of the KMF||graphite full-cells in (a) DPGDME, (b) DPGMPE, and (c) EC/DEC electrolytes at 0.33 C.

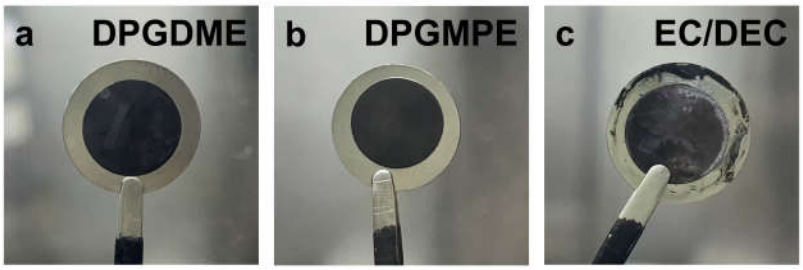

Figure S18. Optical images of the graphite anode after cycling in the KMF||graphite cells with (a) DPGDME, (b) DPGMPE, and (c) EC/DEC electrolytes.

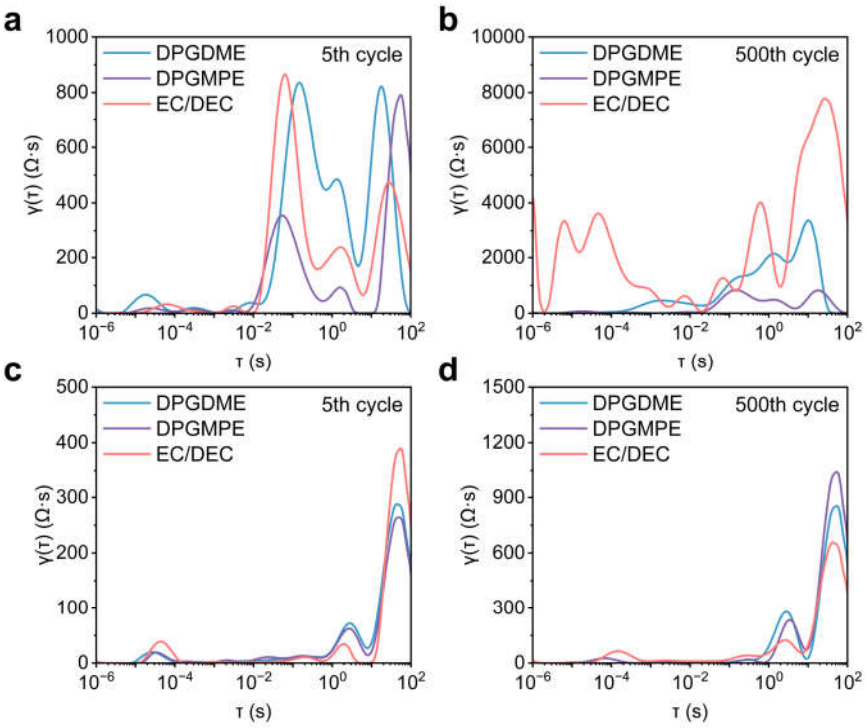

Figure S19. EIS of symmetric cells with electrodes harvested from cycled full-cells: (a, b) graphite anode and (c, d) KMF cathode after 5 and 500 cycles in DPGDME, DPGMPE, and EC/DEC electrolytes.

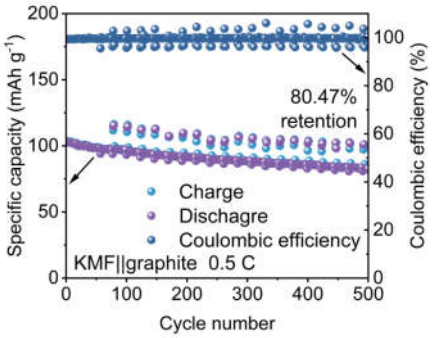

Figure S20. Cycling performance of the KMF||graphite full-cells at 0.5 C with intermittent 24-hour rest periods and two recovery cycles at 0.1 C every 20 cycles in the DPGMPE electrolyte.

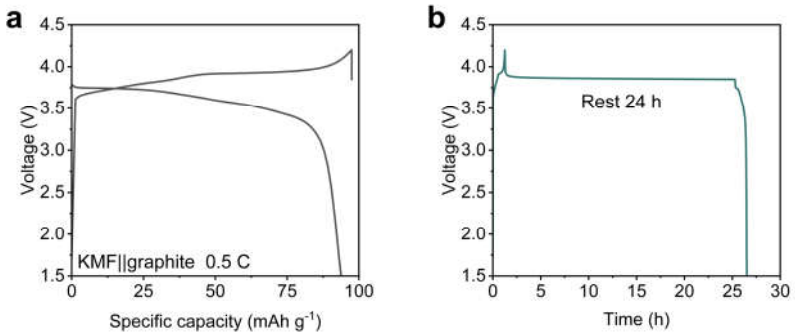

Figure S21. Galvanostatic charge–discharge curves of the KMF||graphite full-cells in the DPGMPE electrolyte at 0.5 C, measured after 77 cycles followed by a 24-hour rest after charge. The curves are plotted versus (a) specific capacity and (b) time.

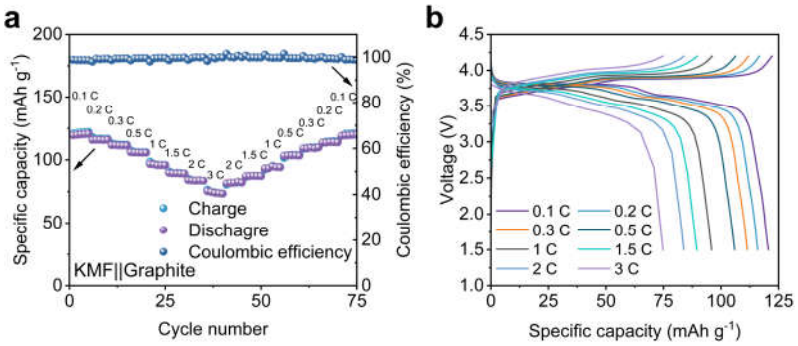

Figure S22. (a) Rate performance and (b) the corresponding charge-discharge curves of the KMF||graphite cells in the DPGMPE electrolyte at various constant charge-discharge rates (0.1 C-3 C).

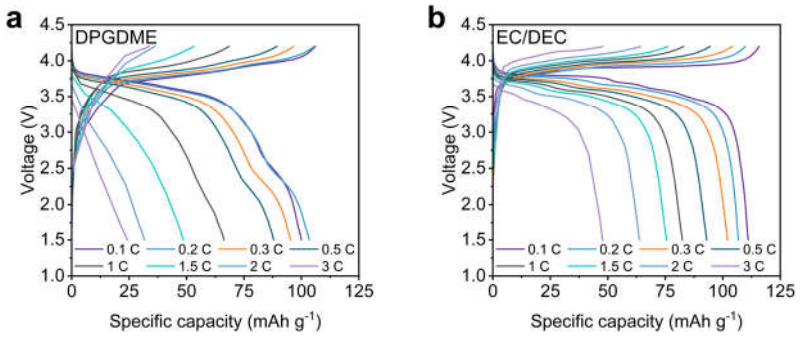

Figure S23. Rate performance of the KMF||graphite full-cells with the (a) DPGDME and (b) EC/DEC electrolytes at various constant charge-discharge rates (0.1 C-3 C).

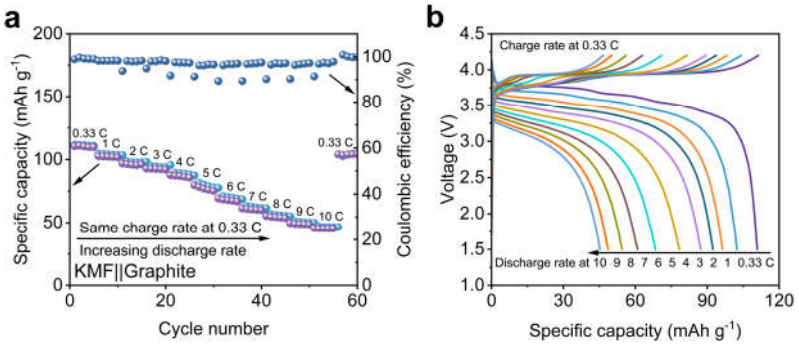

Figure S24. (a) Rate performance and (b) the corresponding charge-discharge curves of the KMF||graphite cells in the DPGMPE electrolyte at a 0.33 C charge rate and various discharge rates (0.33 C-10 C).

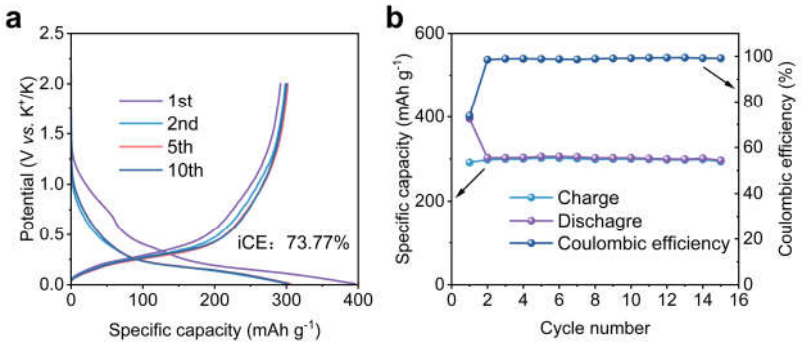

Figure S25. (a) Galvanostatic charge-discharge curves and (b) cycling stability of the HC||K cells in the DPGMPE electrolyte at 0.1 C (1 C=300 mA g^{-1}).

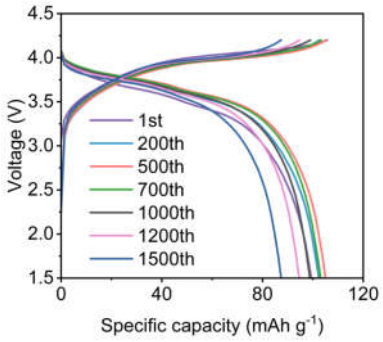

Figure S26. Galvanostatic charge-discharge curves of the KMF||HC full-cells in the DPGMPE electrolyte at 0.5 C.

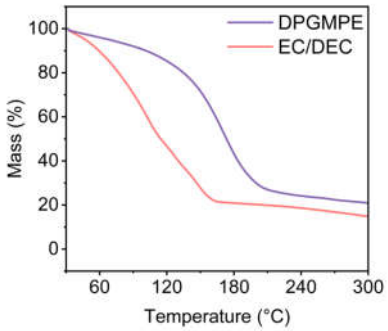

Figure S27. Thermogravimetric analyses (TGA) for the DPGMPE and EC/DEC electrolytes in an Ar atmosphere.

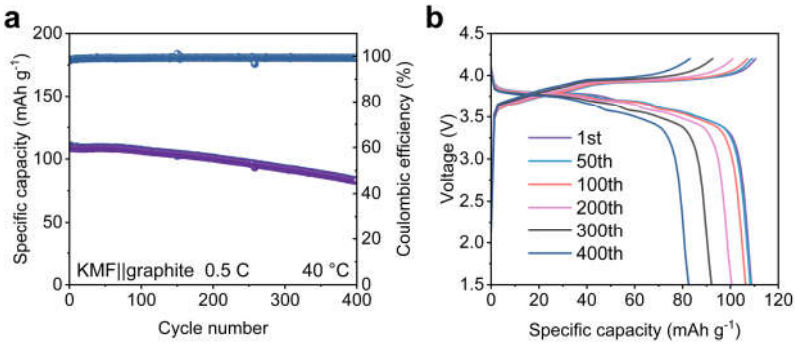

Figure S28. Cycling performances and corresponding voltage profiles of the KMF||graphite full-cells in the DPGMPE electrolyte at 0.5 C under 40 °C.

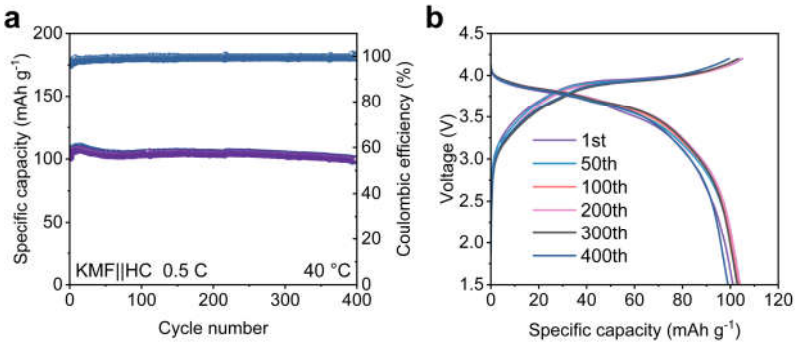

Figure S29. Cycling performances and corresponding voltage profiles of the KMF||HC full-cells in the DPGMPE electrolyte at 0.5 C under 40 °C.

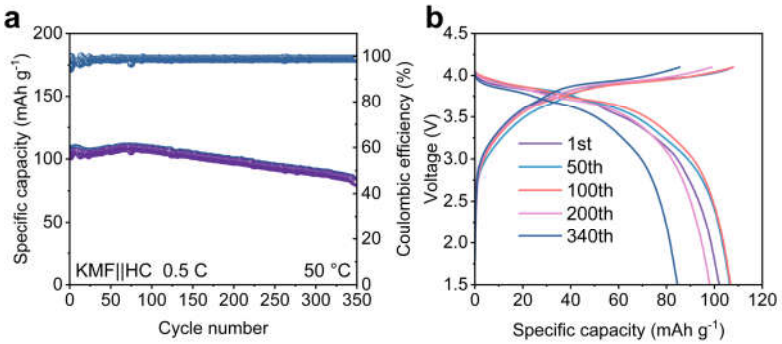

Figure S30. Cycling performances and corresponding voltage profiles of the KMF||HC full-cells in the DPGMPE electrolyte at 0.5 C under 50 °C.

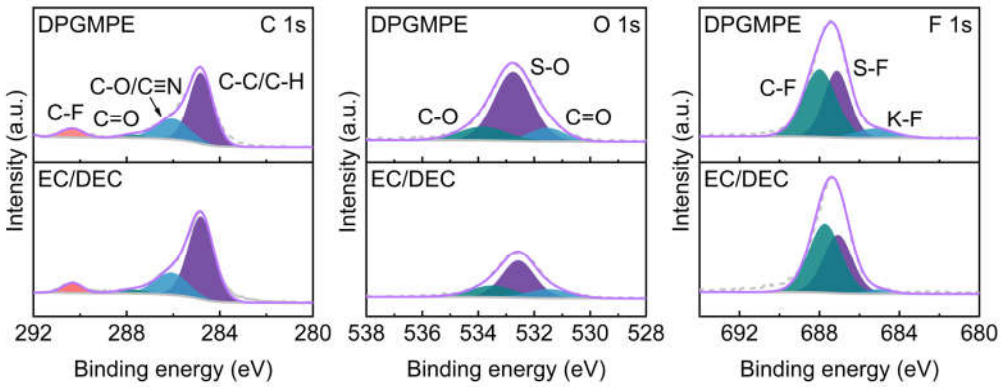

Figure S31. C 1s, O 1s, and F 1s spectra of the KMF cathode after cycling in the DPGMPE and EC/DEC electrolytes.

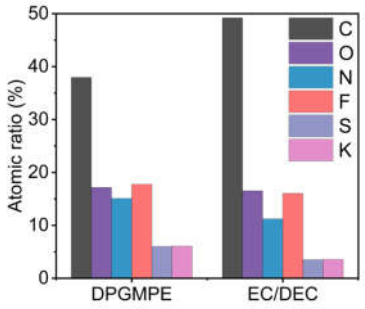

Figure S32. Surface atomic concentrations of the KMF cathode after cycling in the DPGMPE and EC/DEC electrolytes, as determined by XPS.

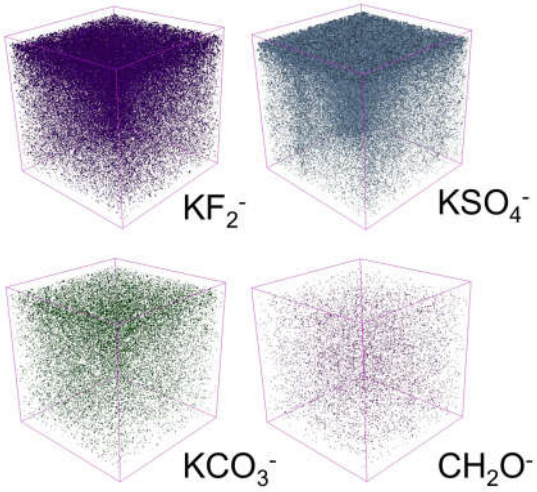

Figure S33. ToF-SIMS 3D reconstruction images for the KMF cathode after cycling in the DPGMPE electrolyte.

Table S1. The density, flash point, melting point, boiling point, and vapor pressure of different electrolyte solvents.

Solvent	Density (g cm^{-3})	Flash point (°C)	Melting point (°C)	Boiling point (°C)	Vapor pressure (hPa)
Diethylene glycol dimethyl ether (DEGDME)	0.943	57	-64	162	3.99 at 20 °C
Diethylene glycol ethyl methyl ether (DEGEME)	0.925	82	-	-	-
Diethylene glycol diethyl ether (DEGDEE)	0.909	67	-44	180	0.7 at 20 °C
Diethylene glycol dibutyl ether (DEGDBE)	0.885	118	-60	256	< 0.01 at 20 °C
Dipropylene glycol dimethyl ether (DPGDME)	0.902	65	-71	175	-
Dipropylene glycol methyl propyl ether (DPGMPE)	0.901	92	-62	197	0.11 at 20 °C
1,2-Dimethoxyethane (DME)	0.87	5	-58	85	87 at 25 °C
Tetrahydrofuran (THF)	0.89	-21.2	-108.44	65	170 at 20 °C
1,4-Dioxane (1,4-DX)	1.03	11	11.8	100	36 at 20 °C
1,3-Dioxane (1,3-DX)	1.03	5	-45	105	-
1,3-Dioxolane (DOL)	1.06	-3	-95	75	93 at 20 °C
Ethylene carbonate (EC)	1.321	143	35	243	< 1 at 20 °C
Dimethyl carbonate (DMC)	1.06	16	2	86	24 at 21.1 °C
Ethyl methyl carbonate (EMC)	1.01	22	-55	101	43 at 25 °C
Diethyl carbonate (DEC)	0.975	25	-43	125	13 at 23.8 °C
Propylene carbonate (PC)	1.2	132	-55	241.8	0.06 at 25 °C

2-Methyltetrahydrofuran (2-MeTHF)	0.855	-10	-136	78	136 at 20 °C
1,2-Diethoxyethane (DEE)	0.842	22	-74	121	13 at 20 °C
1,2-Dimethoxypropane (DMP)	0.855	1	-	96	53.3 at 20 °C
Tetrahydropyran (THP)	0.881	-16	-45	88	-
Triethylene glycol dimethyl ether (TEGDME)	0.986	113	-45	216	0.027 at 20 °C
Tetraethylene glycol dimethyl ether (TREGDME)	1.009	136	-30	275	0.0025 at 20 °C
Dimethoxymethane (DMM)	0.86	-18	-105	41	439.8 at 20 °C
Diemthyl sulfoxide (DMSO)	1.1	87	16	189	0.55 at 20 °C
1,1,2,2-Tetrafluoroethyl-2,2,3,3-tetrafluoropropylether (TTE)	1.5	27	-	92	-
Tetramethyl-1,3-dimethoxydisiloxane (TMMS)	0.891	28.5	-	139	-
Dimethyldimethoxysilane (DMMS)	0.88	10	-	81.4	-
Ethylene sulfite (ES)	1.43	91.7	-	159.1	-
Acetonitrile (AN)	0.786	2	-48	82	-
Fluoroethylene carbonate (FEC)	1.49	102.2	18	212	-
1,1,1-Trifluoro-2-(2,2,2-trifluoroethoxy)ethane (BTFE)	1.4	1	-	-	-

* Data are summarized from the Sigma-Aldrich product datasheet (with the exception of DPGMPE).

Table S2. Comparison of our work with some recently reported electrolytes on PIBs.

Electrolyte	Cathode‖anode	Cycling performance (retention/cycles/ mA g^{-1})	Average discharge voltage (V)	Reference
1 M KFSI DME/MME/OOE	PTCDI‖graphite	83.3%/200/100	< 3	*Nature Sustain.* **2024,** *7* (3), 326-337
3 M KFSI TMP	$K_{0.5}MnO_2$‖soft carbon	79.8%/100/50	< 3	*Adv. Mater.* **2024,** *36* (32), 2405184
4 M KFSI PC	$K_2FeFe(CN)_6$‖Gr	85.7%/1000/200	3 - 3.5	*Energy Environ. Sci.* **2024,** *17* (1), 274-283
2 M KFSI DEM/DME	$K_{0.45}Mn_{0.85}Mg_{0.15}Rb_{0.05}O_2$‖graphite	78.4%/200/200	< 3	*ACS Nano* **2024,** *18* (19), 12512-12523
0.8 M KFSI TFP	$KVPO_4F$‖graphite	87.2%/200/50	> 3.5	*Adv. Funct. Mater.* **2023,** *33* (47), 2305829
0.6 M KFSI TPP/TFP/OHE	FeHCF@rGO‖graphite	92%/187/200	< 3	*Angew. Chem. Inter. Ed.* **2024,** *63* (29), e202405153
2 M KFSI DMP	$KFeFe(CN)_6$‖HC	87.1%/50/50	< 3	*Chem. Eng. J.* **2025,** *524*, 169269
1.5 M KFSI DGM/DBE	$K_{0.51}V_2O_5$‖graphite	73.6%/100/200	< 3	*Natl. Sci. Rev.* **2024,** *11* (11), nwae359
0.5 M KFSI DEE/DBE	PTCDA‖graphite	80.3%/300/200	< 3	*Angew. Chem. Int. Ed.* **2025,** *64* (12), e202422259
1.57 M KFSI TMP/TFTFE	$K_2FeFe(CN)_6$‖graphite	93.1%/100/50	3-3.5	*Energy Stor. Mater.* **2023,** *61*, 102923
2 M KFSI DPGMPE	**$K_2MnFe(CN)_6$‖graphite**	**75.75%/1400/51.15**	**3.61**	**This work**
	$K_2MnFe(CN)_6$‖HC	**80.09%/1500/77.5**	**3.53**	

Table S3. Comparison of our potassium-ion pouch cell' capacity with some recently published reports.

Cathode||anode	Capacity (mAh)	Electrode pretreated	Reference
$K_{0.51}V_2O_5$||graphite	~5.2*	anode	*Natl. Sci. Rev.* **2024,** *11* (11), nwae359
$K_2MnFe(CN)_6$||graphite	12.43	none	*Angew. Chem. Int. Ed.* **2024**, e202415491.
$K_2MnFe(CN)_6$||graphite	~27	none	*Energy Environ. Sci.* **2025,** *18* (16), 7869-7881
PTCDA||graphite	99.6	anode	*Angew. Chem. Inter. Ed.* **2025,** *64* (14), e202421928
PTCDA||graphite	106	anode	*Adv. Energy Mater.* **2023,** *13* (18), 2300453
$K_2MnFe(CN)_6$||graphite	**123.6**	**none**	**This work**

* "~" indicates that the value was estimated from data plots in the references.

SI Reference

1. L. Deng, J. Qu, X. Niu, J. Liu, J. Zhang, Y. Hong, M. Feng, J. Wang, M. Hu, L. Zeng, Q. Zhang, L. Guo and Y. Zhu, *Nature Communications*, 2021, **12**, 2167.
2. S. Dhir, B. Jagger, A. Maguire and M. Pasta, *Nature Communications*, 2023, **14**, 3833.
3. M. J. Frisch, G. W. Trucks, H. B. Schlegel, G. E. Scuseria, M. A. Robb, J. R. Cheeseman, G. Scalmani, V. Barone, G. A. Petersson, H. Nakatsuji, X. Li, M. Caricato, A. V. Marenich, J. Bloino, B. G. Janesko, R. Gomperts, B. Mennucci, H. P. Hratchian, J. V. Ortiz, A. F. Izmaylov, J. L. Sonnenberg, Williams, F. Ding, F. Lipparini, F. Egidi, J. Goings, B. Peng, A. Petrone, T. Henderson, D. Ranasinghe, V. G. Zakrzewski, J. Gao, N. Rega, G. Zheng, W. Liang, M. Hada, M. Ehara, K. Toyota, R. Fukuda, J. Hasegawa, M. Ishida, T. Nakajima, Y. Honda, O. Kitao, H. Nakai, T. Vreven, K. Throssell, J. A. Montgomery Jr., J. E. Peralta, F. Ogliaro, M. J. Bearpark, J. J. Heyd, E. N. Brothers, K. N. Kudin, V. N. Staroverov, T. A. Keith, R. Kobayashi, J. Normand, K. Raghavachari, A. P. Rendell, J. C. Burant, S. S. Iyengar, J. Tomasi, M. Cossi, J. M. Millam, M. Klene, C. Adamo, R. Cammi, J. W. Ochterski, R. L. Martin, K. Morokuma, O. Farkas, J. B. Foresman and D. J. Fox, *Journal*, 2016.
4. P. J. Stephens, F. J. Devlin, C. F. Chabalowski and M. J. Frisch, *The Journal of Physical Chemistry*, 1994, **98**, 11623-11627.
5. T. Lu and F. Chen, 2012, **33**, 580-592.
6. W. Humphrey, A. Dalke and K. Schulten, *Journal of Molecular Graphics*, 1996, **14**, 33-38.
7. S. Plimpton, *Journal of Computational Physics*, 1995, **117**, 1-19.
8. K. P. Jensen and W. L. Jorgensen, *Journal of Chemical Theory and Computation*, 2006, **2**, 1499-1509.
9. J. N. Canongia Lopes, K. Shimizu, A. A. H. Pádua, Y. Umebayashi, S. Fukuda, K. Fujii and S.-i. Ishiguro, *The Journal of Physical Chemistry B*, 2008, **112**, 9449-9455.
10. L. S. Dodda, I. C. d. Vaca, J. Tirado-Rives and W. L. J. N. A. R. Jorgensen, 2017, **45**, W331 - W336.
11. L. Martínez, R. Andrade, E. G. Birgin and J. M. Martínez, 2009, **30**, 2157-2164.
12. A. I. Jewett, D. Stelter, J. Lambert, S. M. Saladi, O. M. Roscioni, M. Ricci, L. Autin, M. Maritan, S. M. Bashusqeh, T. Keyes, R. T. Dame, J.-E. Shea, G. J. Jensen and D. S. Goodsell, *Journal of Molecular Biology*, 2021, **433**, 166841.
13. V. Ponnuchamy, *Chemical Physics Letters*, 2020, **754**, 137707.
14. K. Momma and F. Izumi, *Journal of Applied Crystallography*, 2011, **44**.